sensors

MDPI

Article

Design and Experiment of a Portable Near-Infrared Spectroscopy Device for Convenient Prediction of Leaf Chlorophyll Content

Longjie Li [1], Junxian Guo [2,*], Qian Wang [1], Jun Wang [1], Ya Liu [1] and Yong Shi [1]

[1] College of Mechanical and Electrical Engineering, Xinjiang Agricultural University, Urumqi 830052, China; lidelongjie@163.com (L.L.); hebau_wangqian@163.com (Q.W.); 320232352@xjau.edu.cn (J.W.); zztyly@163.com (Y.L.); shiyong19860324@163.com (Y.S.)

[2] Key Laboratory of Xinjiang Intelligent Agricultural Equipment, Urumqi 830052, China

* Correspondence: junxianguo@163.com

Abstract: This study designs a spectrum data collection device and system based on the Internet of Things technology, aiming to solve the tedious process of chlorophyll collection and provide a more convenient and accurate method for predicting chlorophyll content. The device has the advantages of integrated design, portability, ease of operation, low power consumption, low cost, and low maintenance requirements, making it suitable for outdoor spectrum data collection and analysis in fields such as agriculture, environment, and geology. The core processor of the device uses the ESP8266-12F microcontroller to collect spectrum data by communicating with the spectrum sensor. The spectrum sensor used is the AS7341 model, but its limited number of spectral acquisition channels and low resolution may limit the exploration and analysis of spectral data. To verify the performance of the device and system, this experiment collected spectral data of Hami melon leaf samples and combined it with a chlorophyll meter for related measurements and analysis. In the experiment, twelve regression algorithms were tested, including linear regression, decision tree, and support vector regression. The results showed that in the original spectral data, the ETR method had the best prediction effect at a wavelength of 515 nm. In the training set, $RMSE_c$ was 0.3429, and R_c^2 was 0.9905. In the prediction set, $RMSE_p$ was 1.5670, and R_p^2 was 0.8035. In addition, eight preprocessing methods were used to denoise the original data, but the improvement in prediction accuracy was not significant. To further improve the accuracy of data analysis, principal component analysis and isolation forest algorithm were used to detect and remove outliers in the spectral data. After removing the outliers, the RFR model performed best in predicting all wavelength combinations of denoised spectral data using PBOR. In the training set, $RMSE_c$ was 0.8721, and R_c^2 was 0.9429. In the prediction set, $RMSE_p$ was 1.1810, and R_p^2 was 0.8683.

Keywords: Internet of Things technology; spectral data analysis; chlorophyll content prediction; regression algorithms; data preprocessing

Citation: Li, L.; Guo, J.; Wang, Q.; Wang, J.; Liu, Y.; Shi, Y. Design and Experiment of a Portable Near-Infrared Spectroscopy Device for Convenient Prediction of Leaf Chlorophyll Content. *Sensors* **2023**, *23*, 8585. https://doi.org/10.3390/s23208585

Academic Editor: Francesca Antonucci

Received: 19 September 2023
Revised: 10 October 2023
Accepted: 18 October 2023
Published: 19 October 2023

1. Introduction

With the development and popularization of Internet of Things (IoT) technology, the application scope of sensors and devices is becoming increasingly wide [1–4]. Spectrum data can reflect the characteristics and properties of substances [5], while providing object recognition and classification information [6]. In the field of agriculture, the collection and analysis of spectrum data are of great significance for nutrient management and growth monitoring of Hami melon crops [7]. Hami melon is an important economic crop [8], and photosynthesis is crucial for ensuring healthy growth and high yield of plants [9]. Chlorophyll, as an important photosynthetic pigment in plants [10], is closely related to the photosynthetic rate and growth status of plants [11,12]. By measuring and analyzing spectrum data of plants, critical information such as chlorophyll content can be obtained

non-destructively [13]. Jeremy Aditya Prananto first evaluated the ability of handheld near-infrared spectrometers to predict nutrient content in dried and ground cotton leaf samples, demonstrating that handheld near-infrared spectrometers are a practical choice for accurately measuring leaf nutrient concentration [14]. Lihua Liu found that near-infrared spectroscopy can be used as an alternative method for real-time quantitative and monitoring of chlorophyll during the processing of Tiancha [15], providing scientific guidance for agricultural production. Jianfeng Zhang developed a new method for estimating winter wheat leaf chlorophyll content based on visible and near-infrared sensors [16]. Yu-Jie Wang used a miniature near-infrared spectrometer to evaluate the pigment content of two field tea trees. A miniature near-infrared system based on a smartphone can quickly, non-destructively, and inexpensively diagnose plant nutrition status [17]. Xiu Jin used a handheld miniature near-infrared spectrometer to analyze the nitrogen, phosphorus, and potassium content of nutrient-deficient pear leaf samples, with this method able to quickly predict nutrient deficiency during the cultivation period of pear leaves [18], promoting crop quality and yield improvement [19]. However, traditional spectral data collection and analysis processes have some shortcomings. For example, traditional spectral data collection methods require the use of complex fiber optic cables to transmit spectral information and rely on heat-generating light source equipment and spectral analyzer equipment to collect data with a computer. The large size of the entire device is inconvenient for outdoor collection operations, and the user interface is simple and cannot meet the requirements of data visualization and real-time interaction.

To solve the above problems, this study proposes a spectrum data collection device and system based on IoT technology (see Appendix A for details). Through the combination of cloud servers, collection devices, and interactive interfaces, the system achieves automatic collection, storage, and data visualization of spectral data. The cloud server deploys a series of necessary software services using Docker containerization technology to achieve efficient data reception, secure storage, and flexible interaction. The collection device integrates advanced microcontrollers and spectral sensors to achieve accurate collection and transmission of spectral data. The interactive interface uses Websocket technology to achieve real-time synchronization of front-end and back-end data and user visualization operations.

This study demonstrates non-destructive detection of chlorophyll content in muskmelon leaves. By collecting spectral data and chlorophyll content measurements of muskmelon plants at different growth stages and nutrient states, a prediction model can be established, and chlorophyll content can be predicted by analyzing the spectral data of new samples [20]. Such a prediction model provides important reference for agricultural production, helping farmers and agricultural experts adjust fertilization and nutrient management strategies in a timely manner [21], and maximizing the yield and quality of muskmelon [22]. The experiment proves that the spectral data collected using IoT technology can accurately predict the chlorophyll content of leaves through various data processing and analysis. At the same time, the design of the interactive interface enables users to conveniently operate and explore spectral data and obtain real-time collection results. Therefore, the research results have important theoretical significance and practical application value, providing a new solution for the collection and analysis of spectral data, and providing strong support for practical application in agriculture, environmental monitoring, and other related fields.

2. Overall Design of the Device

As shown in Figure 1, the collection device ensures that equidistant spectral data can be obtained every time through the spectral sensor (6) and leaf fixing plate (7). The operation of the device mainly depends on the cloud server, collection device, and interactive interface. The cloud server adopts Docker containerization technology to deploy the EMQX, Node-RED, InfluxDB, and Flask environments, realizing the reception, storage, and data interaction of the data input by the web page users and the spectral data collected by the collection device. The collection device uses the ESP8266-12F microcontroller (hereinafter referred to as the microcontroller) as the core processor, communicates with the spectral

sensor to obtain spectral data, and transmits the collected data to the cloud server through WiFi wireless network. The interactive interface uses Websocket technology to achieve real-time synchronization of front-end and back-end data, and visualizes the data through chart functions, providing intuitive data analysis and display functions.

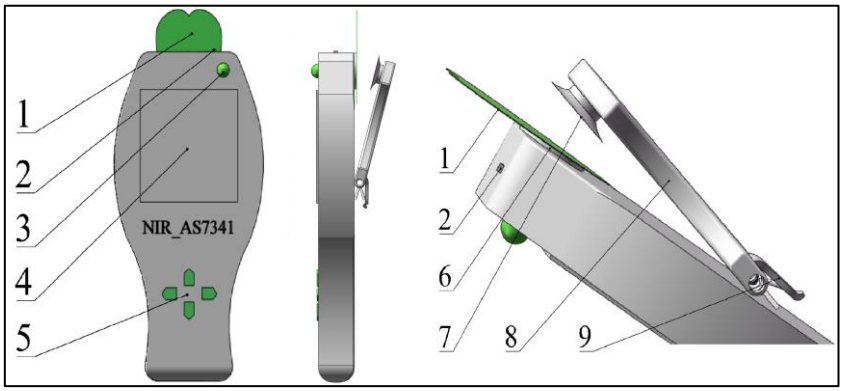

Figure 1. Structure of the Acquisition Device. 1. Leaf blade; 2. power switch; 3. indicator light; 4. display screen; 5. function keys; 6. AS7341; 7. fixing plate; 8. force arm; 9. switch.

2.1. Deployment of IoT Server

As shown in Figure 2, the server is configured with one core CPU, 2 GB memory, 40 GB system disk, and 1 Mbps public network bandwidth, running on Ubuntu 16.04.6 LTS x86_64. EMQX is responsible for handling the access to MQTT communication devices and forwarding topic data to ensure efficient data transmission. Node-RED serves as a flow orchestration tool, listening to and capturing the spectrum data collected by the AS7341 spectrum device and the data input by the user on the web page in real-time and forwarding them to the InfluxDB database for reliable data storage. Meanwhile, Flask is used to subscribe to real-time spectrum data in the MQTT server and the data saved in the final database and transmit said data to the front-end for visualization display through WebSocket.

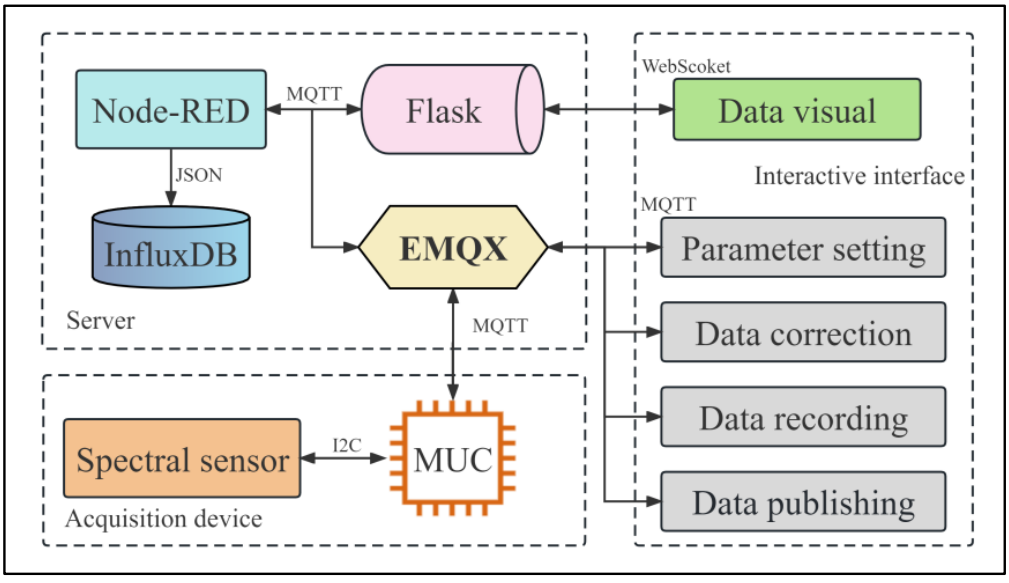

Figure 2. Overall functional architecture.

2.2. Spectral Acquisition Device

The spectral acquisition device, as shown in Figure 3, uses a two-layer PCB circuit board without copper for testing. The device is powered by a 5 V power bank, and the

spectral sensor used is the AS7341, with a data acquisition channel covering a range of 415 nm to 940 nm. The collected spectral data are efficiently processed by the microcontroller through I^2C communication. As shown in Figure 4, the microcontroller packages the sensor data and wirelessly transmits it to the cloud server via a shared network WiFi connection with a mobile phone (see Appendix B for details). Users can view the real-time visualization of the latest collected spectral data through a web interface. At the same time, the microcontroller receives information on light intensity, acquisition times, and data calibration instructions from the server. By using the light intensity information to control the current of the LED, the brightness of the LED can be adjusted. Meanwhile, by setting the original spectral acquisition times based on the acquisition times information, the average value calculation is performed to improve the reliability and accuracy of the data. By receiving spectral calibration instructions, the data correction and compensation parameters are used to adjust the whiteboard spectral curve to the same level, ensuring the accuracy and consistency of the data.

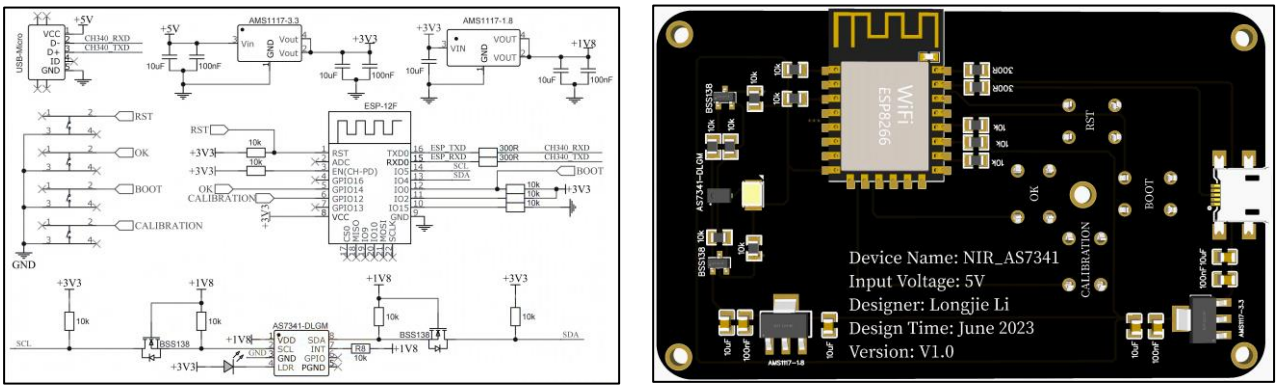

(**a**) (**b**)

Figure 3. Spectral acquisition device. (**a**) Schematic diagram; (**b**) PCB diagram.

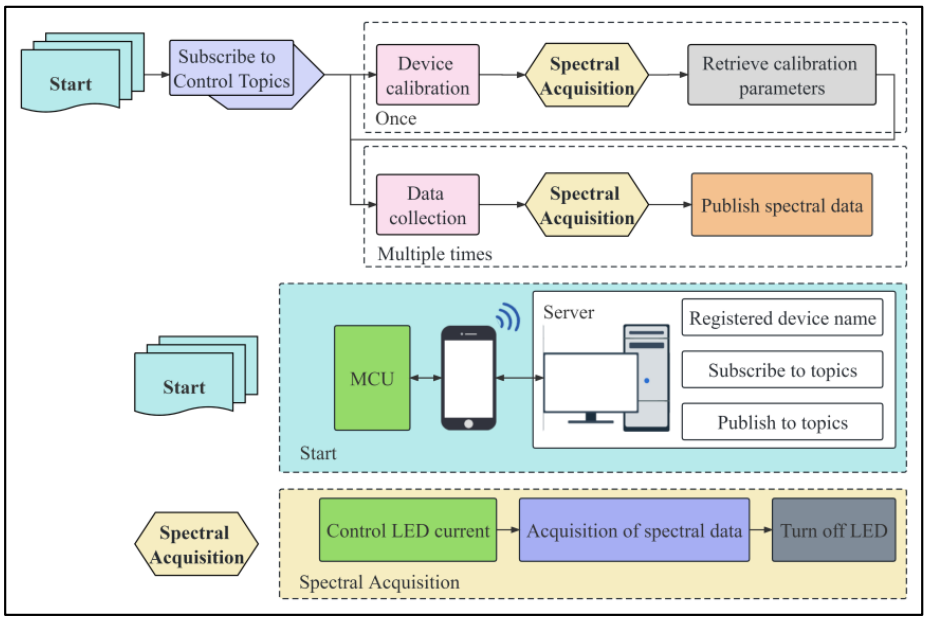

Figure 4. Spectral acquisition flowchart.

2.3. Interactive Interface Design

The collection interface is shown in Figure 5. The back-end uses Flask to establish a communication connection with the MQTT server, subscribes to the spectral data sent by

the spectral acquisition device, and uses WebSocket to transmit the spectral data to the front-end for real-time rendering and display. The front-end is responsible for receiving and rendering the spectral data sent by the back-end and for providing users with the function to input experimental sample numbers, leaf temperature, and chlorophyll data. The front-end sends the user-input data to the back-end through an interface. After receiving the data submitted by the user through the web page, the back-end splices it with the latest spectral data, packages it, and sends it to the MQTT server for data forwarding and storage in the InfluxDB database. The latest database data are visualized and displayed in the front-end, allowing operators to confirm whether their submitted data have been successfully saved. In addition, the functionality provided by InfluxDB allows for the download of saved data, including combined data of user-submitted data and spectral data, reducing the workload of experimental personnel in secondary data statistics, and providing an efficient and reliable data processing and analysis environment for them.

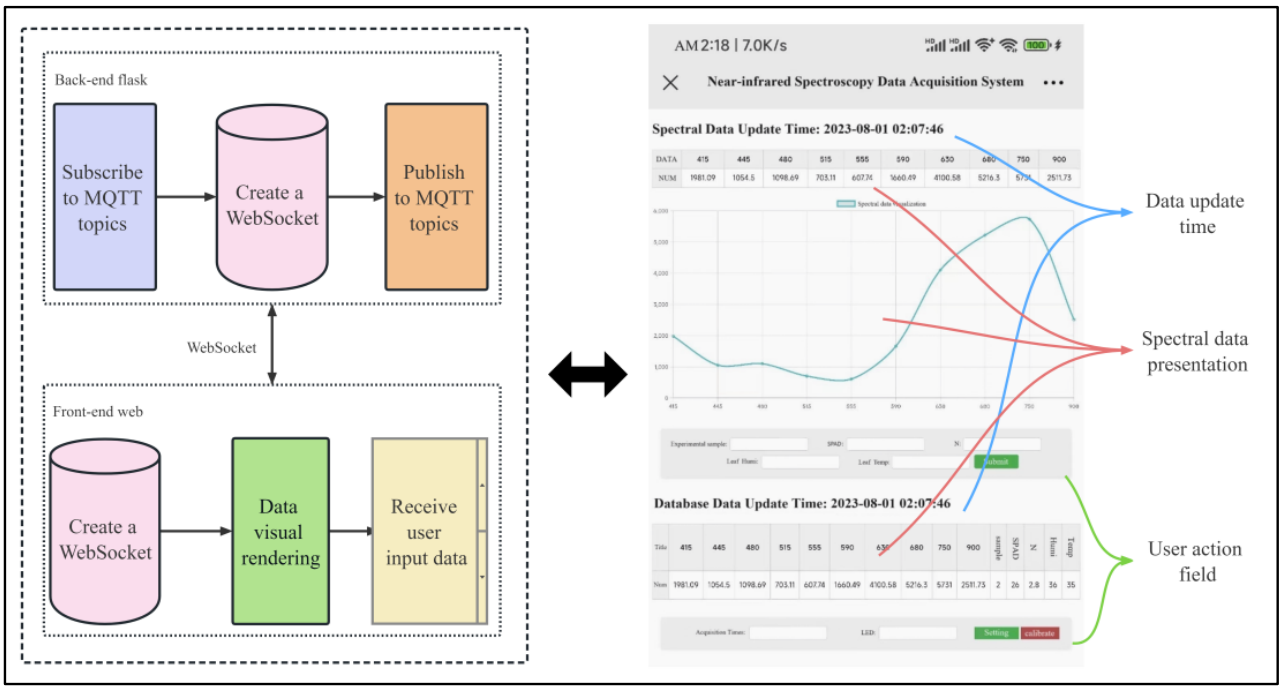

Figure 5. Interactive interface design.

2.4. Data Collection

The experiment was conducted at the experimental field of Xinjiang Academy of Agricultural Sciences, with longitude of 87.476325 and latitude of 43.949915. A Top Cloud-agri TYS-4N chlorophyll meter was selected, with a measurement range of 0.0–99.9 SPAD and an accuracy of ±1.0 SPAD. The SPAD values of the leaves of Hami melon were measured, avoiding measuring over the thick veins to ensure the accuracy of the measurement results [23]. The SPAD values and spectral data of 100 different plant leaf samples were measured outdoors, and the collected spectral data are shown in Figure 6a. Before collecting spectral data, the hardware acquisition parameters need to be set in the web setting area of the collection device. In the "Acquisition Times" position on the web page, the average collection times should be set to 3, and the LED current size should also be set to 3 in the "LED" position. After completing these parameter settings, click the "Setting" button to submit the set parameters. During the subsequent spectral data collection, three original average spectral data points of the leaf samples under fixed light intensity can be obtained [24].

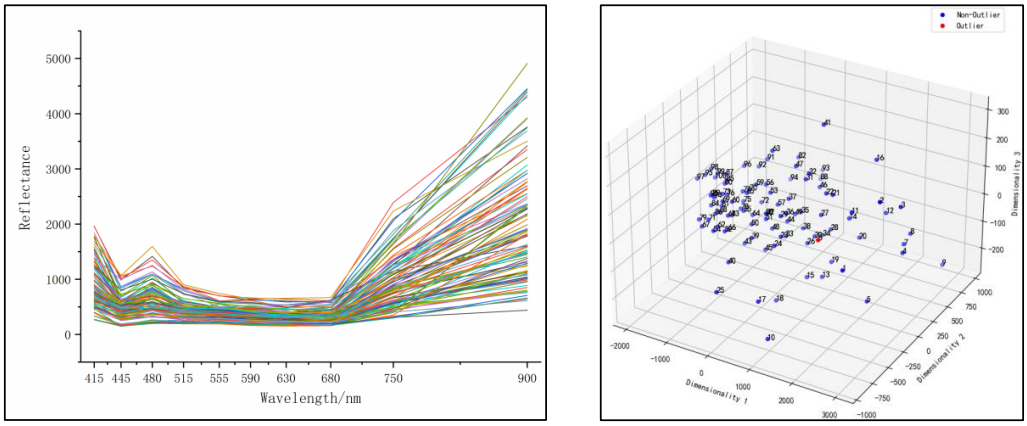

(**a**) (**b**)

Figure 6. Raw spectral data. (**a**) Data curves; (**b**) anomaly removal.

3. Results

3.1. Prediction of Raw Spectral Data

The original spectral data are shown in Figure 6a. The entire dataset was randomly divided into a 70:30 ratio for model training and prediction, respectively. Twelve regression algorithms were used to analyze the spectral data and SPAD values, including linear regression (LR) [25], K-nearest neighbor regression (KNN) [26], support vector regression (SVR) [27], ridge regression (RR) [28], Lasso regression (Lasso) [29], decision tree regression (DTR) [30], extremely randomized tree regression (ETR) [31], random forest regression (RFR) [32], AdaBoost regression (ABR) [33], gradient boosting regression (GBR) [34], bagging regression (BAR) [35], and partial least squares regression (PLSR) [36] (see Appendix C for details). For each collection band and all band combinations between 415 nm and 940 nm, the twelve regression algorithms were used for analysis and prediction. The best prediction results for each regression analysis are shown in Table 1. It was found that ETR, RFR, and BAR performed well in predicting SPAD values at a wavelength of 515 nm, with ETR attaining the best prediction performance. On the training set, the $RMSE_c$ of ETR was 0.3429 and R_c^2 was 0.9905. On the prediction set, the $RMSE_p$ of ETR was 1.5670 and R_p^2 was 0.8035. The model prediction performance is shown in Figure 9a.

Table 1. Original spectrum and SPAD analysis.

Forecasting Method	Wavelength (nm)	Training Set		Prediction Set	
		$RMSE_c$	R_c^2	$RMSE_p$	R_p^2
LR	590	1.9273	0.6987	2.0030	0.6691
KNN	515	1.5182	0.8130	1.6608	0.7792
SVR	515	1.8824	0.7126	1.8471	0.7269
RR	590	1.9273	0.6987	2.0330	0.6691
Lasso	590	1.9273	0.6987	2.0330	0.6691
DTR	515	0.3429	0.9905	1.7449	0.7563
ETR	**515**	**0.3429**	**0.9905**	**1.5670**	**0.8035**
RFR	515	0.7062	0.9595	1.5798	0.8002
ABR	515	1.1206	0.8981	1.6480	0.7826
GBR	515	0.4692	0.9821	1.6986	0.7690
BAR	515	0.8010	0.9480	1.5777	0.8008
PLSR	590	1.9273	0.6987	2.0330	0.6691

3.2. Spectral Data Denoising Analysis

Considering the noise interference from environmental light during the collection of original spectral data from leaf samples [37], eight widely used preprocessing methods were employed to eliminate the effects of scattering and noise on the original data. These methods include Multiplicative Scatter Correction (MSC) [38], Standard Normal Variate (SNV) [39], Discrete Wavelet Transform (DWT) [40], Savitzky-Golay (SG) smoothing [41],

MinMax scaling (MinMax) [42], Outlier Detection (OD) [43], Percentile-based outlier removal (PBOR) [44], and Continuum Removal (CR) [45]. The preprocessed spectral curves are shown in Figure 7. To evaluate the effects of these eight denoising preprocessing methods on prediction accuracy, ETR, RFR, and BAR, the three regression algorithms with the highest prediction accuracy in the original spectra, were used to perform regression analysis on each denoised spectrum. The analysis results are shown in Table 2. By comparing the regression results of each denoising method with the $RMSE_c$, R_c^2, $RMSE_p$, and R_p^2 values in Table 1, it was found that DWT and OD showed a trend of decreasing prediction accuracy, while the other preprocessing methods did not significantly improve the prediction accuracy.

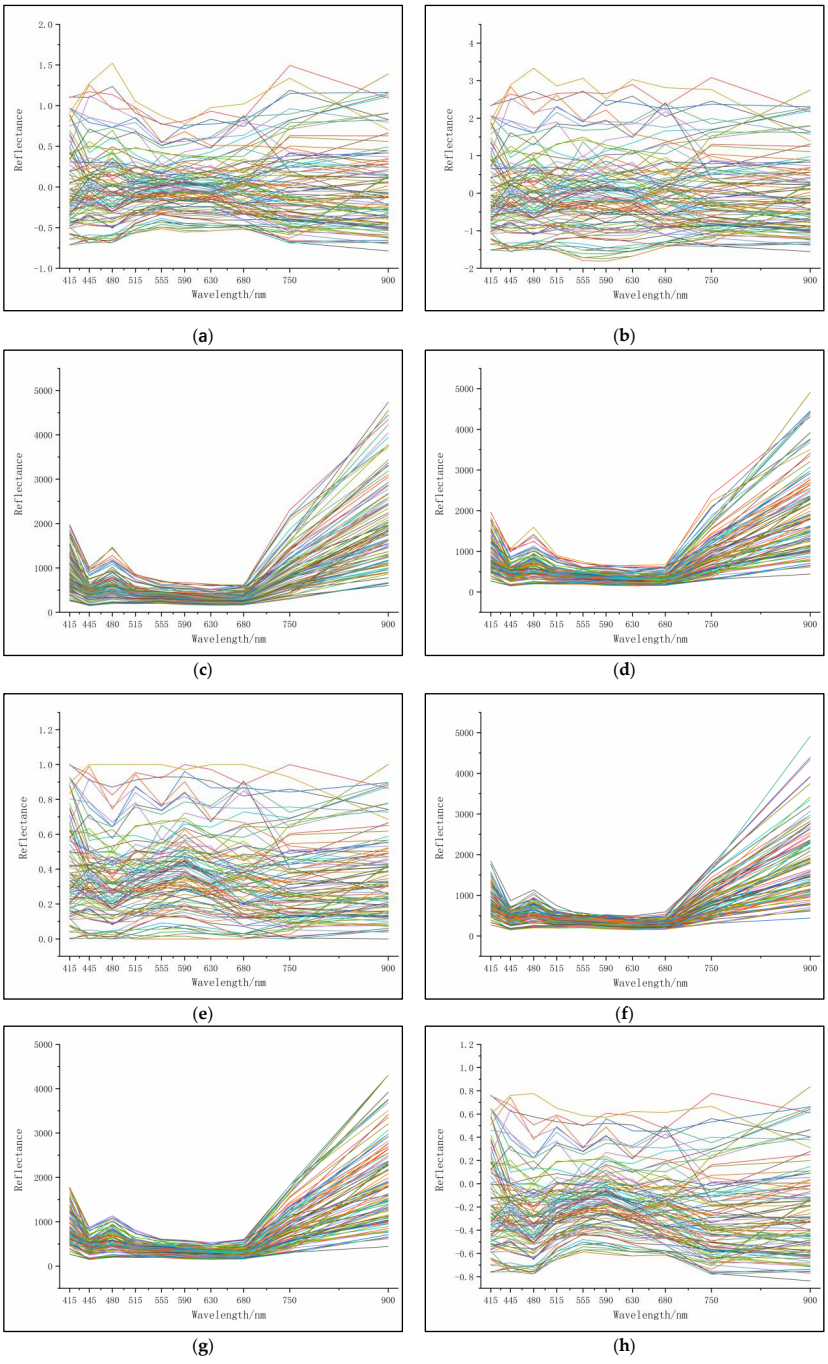

Figure 7. Spectral data noise reduction processing. (**a**) MSC; (**b**) SNV; (**c**) DWT; (**d**) SG; (**e**) MinMax; (**f**) OD; (**g**) PBOR; (**h**) CR.

Table 2. Noise reduction analysis of spectral data.

Pretreatment Method	Forecasting Method	Wavelength (nm)	Training Set		Prediction Set	
			$RMSE_c$	R_c^2	$RMSE_p$	R_p^2
MSC	**ETR**	**515**	**0.3429**	**0.9905**	**1.5670**	**0.8035**
	RFR		0.7061	0.9596	1.5826	0.7995
	BAR		0.8010	0.9480	1.5777	0.8008
SNV	**ETR**	**515**	**0.3429**	**0.9905**	**1.5670**	**0.8035**
	RFR		0.7061	0.9596	1.5826	0.7995
	BAR		0.8010	0.9480	1.5777	0.8008
DWT	ETR	555	0.0720	0.9996	2.3676	0.5513
	RFR	590	0.7567	0.9536	2.2347	0.6002
	BAR	555	1.0597	0.9089	2.2184	0.6061
SG	**ETR**	**515**	**0.3429**	**0.9905**	**1.5670**	**0.8035**
	RFR		0.7062	0.9595	1.5798	0.8002
	BAR		0.8010	0.9480	1.5777	0.8008
MinMax	**ETR**	**515**	**0.3429**	**0.9905**	**1.5670**	**0.8035**
	RFR		0.7044	0.9598	1.5798	0.8002
	BAR		0.7989	0.9482	1.5777	0.8008
OD	ETR	590	0.1737	0.9971	1.8834	0.6074
	RFR		0.7179	0.9508	1.7394	0.6651
	BAR		0.8133	0.9369	1.7986	0.6419
PBOR	ETR	515	0.3618	0.9894	1.5813	0.7998
	RFR		0.7106	0.9590	1.5853	0.7988
	BAR		0.8079	0.9471	1.5679	0.8032
CR	**ETR**	**515**	**0.3429**	**0.9905**	**1.5670**	**0.8035**
	RFR		0.7061	0.9596	1.5826	0.7995
	BAR		0.8010	0.9480	1.5777	0.8008

3.3. Data Dimensionality Reduction and Outlier Removal

To eliminate the interference of abnormal samples in the denoised and original spectral data, Principal Component Analysis (PCA) was used to reduce the dimensionality of the data [46], with a final dimension of three and projection onto a three-dimensional space. An Isolation Forest (IF) algorithm was used to detect and distinguish abnormal values based on the distribution of each sample point in the three-dimensional space [47]. The classification results of the original spectral data and the denoised spectral data are shown in Figures 6b and 8, respectively. After removing the abnormal values from the original and denoised spectral data, ETR, RFR, and BAR regression analysis were performed separately. The specific analysis results are shown in Table 3, and the judgment analysis was compared with the $RMSE_c$, R_c^2, $RMSE_p$, and R_p^2 of Table 1. The prediction accuracy of ETR decreased significantly, while in RFR and BAR, the prediction accuracy increased significantly. Among them, the effect of RFR was the best. Compared with the highest precision model without removing the abnormal values, the $RMSE_p$ decreased from 1.5670 to 1.3456, and the R_p^2 increased from 0.8035 to 0.8358. After removing the abnormal values from the denoised spectral data, all the denoising data prediction accuracies improved, and RFR showed the best accuracy in predicting all bands under PBOR denoising. Compared with the highest precision model of the original and denoised spectral data, the $RMSE_p$ decreased from 1.5670 to 1.1810, and the R_p^2 increased from 0.8035 to 0.8683. Therefore, RFR showed the best modeling effect and stability in predicting chlorophyll in all bands under PBOR denoising. The model predictions are shown in Figure 9b.

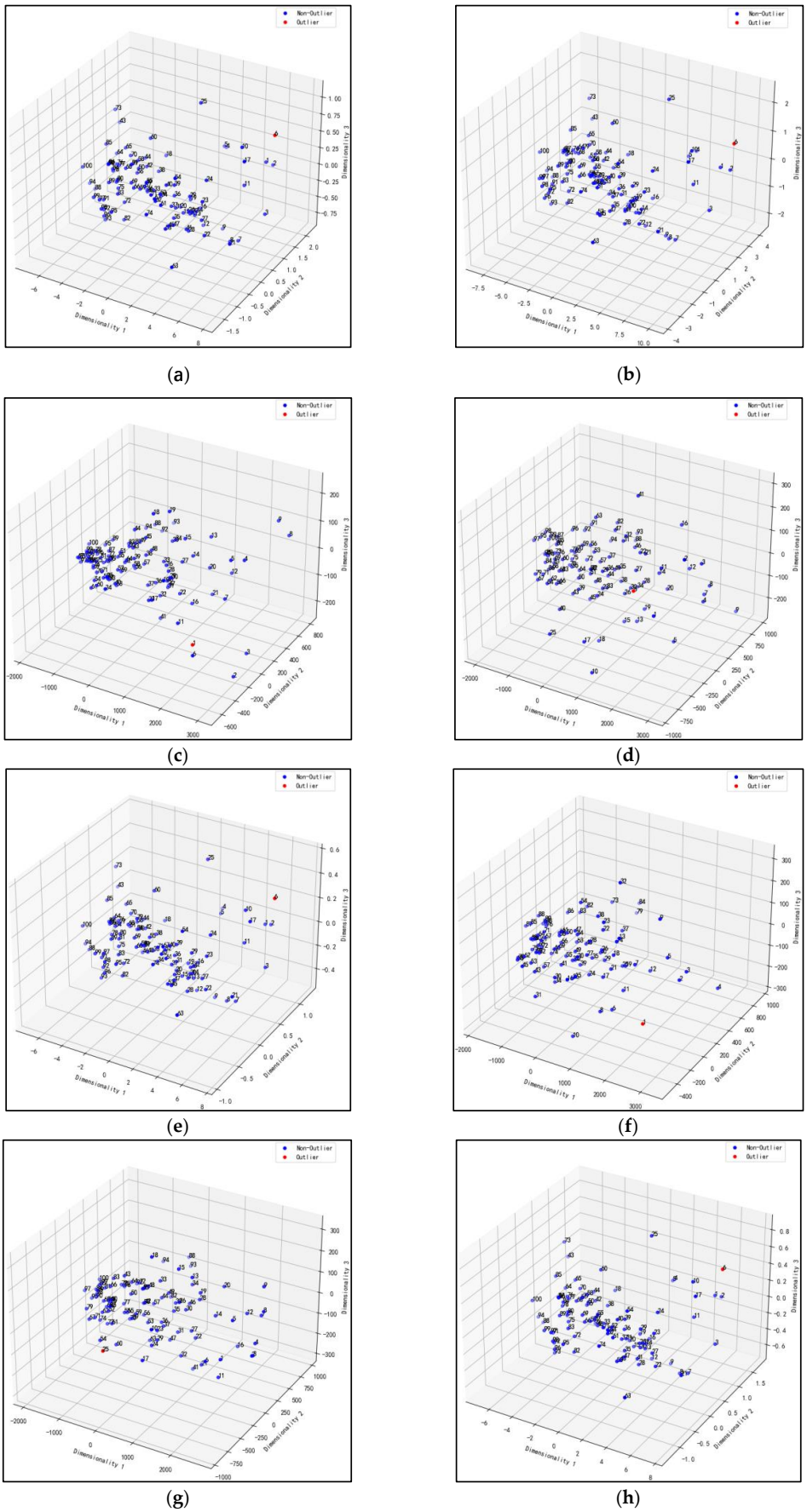

Figure 8. Abnormal value elimination distribution map. (**a**) MSC; (**b**) SNV; (**c**) DWT; (**d**) SG; (**e**) Min-Max; (**f**) OD; (**g**) PBOR; (**h**) CR.

Table 3. Outlier rejection analysis.

Pretreatment Method	Pretreatment Method	Forecasting Method	Wavelength (nm)	Training Set		Prediction Set	
				$RMSE_c$	R_c^2	$RMSE_p$	R_p^2
Non	1	ETR	All	0.1665	0.9978	1.6408	0.7558
		RFR		0.8736	0.9394	1.3456	0.8358
		BAR		1.1249	0.8996	1.3799	0.8273
MSC	1	ETR	515	0.1665	0.9978	1.6408	0.7558
		RFR	All	0.8736	0.9394	1.3467	0.8355
		BAR		1.1249	0.8996	1.3858	0.8258
SNV	1	ETR	515	0.1665	0.9978	1.6408	0.7558
		RFR	All	0.8736	0.9394	1.3456	0.8358
		BAR		1.1249	0.8996	1.3799	0.8273
DWT	1	ETR	590	0.0904	0.9993	2.1442	0.6252
		RFR		0.9712	0.9222	1.8656	0.7162
		BAR		1.1681	0.8874	1.9453	0.6915
SG	1	ETR	515	0.1665	0.9978	1.6408	0.7558
		RFR		0.8736	0.9394	1.3456	0.8358
		BAR		1.1249	0.8996	1.3799	0.8273
MinMax	1	ETR	515	0.1665	0.9978	1.6408	0.7558
		RFR		0.8736	0.9394	1.3461	0.8356
		BAR		1.1249	0.8996	1.3858	0.8258
OD	1	ETR	515	0.5161	0.9719	1.9488	0.6732
		RFR	All	0.7140	0.9462	1.7327	0.7417
		BAR	555	0.9447	0.9059	1.9373	0.6771
PBOR	**1**	ETR	555	0.4962	0.9815	1.4004	0.8148
		RFR	**All**	**0.8721**	**0.9429**	**1.1810**	**0.8683**
		BAR	515	1.0745	0.9133	1.4931	0.7895
CR	1	ETR	515	0.1665	0.9978	1.6408	0.7558
		RFR	All	0.8736	0.9394	1.3467	0.8355
		BAR	All	1.1249	0.8996	1.3858	0.8258

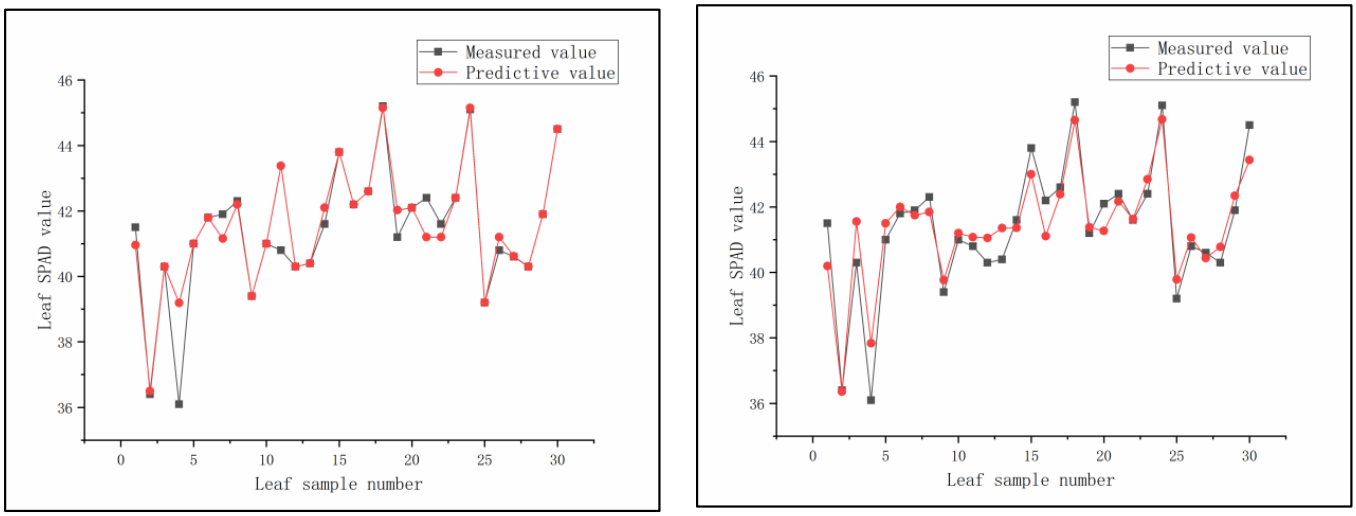

Figure 9. SPAD prediction model. (**a**) Prediction of raw spectra at 515 nm using ETR regression model; (**b**) Prediction of de-noised spectra in all bands of PBOR using RFR regression model.

4. Discussion

This study successfully designed a spectrum data acquisition device and system based on the IoT technology, which integrated the AS7341 spectral sensor and ESP8266 microcontroller to achieve integrated spectrum data acquisition. Compared with traditional spectrometers, the spectrum acquisition device designed in this paper has many advantages and some disadvantages.

Advantages: integrated design. The ESP8266 microcontroller, AS7341 spectral sensor, and LED light source are integrated, which is convenient for outdoor spectrum data collection. At the same time, since there is no exposed signal transmission part, the impact of environmental light is relatively reduced. Portability: it has a small size and weight which render it convenient to carry and use. In addition, there is no need to pay attention to the bending of the optical fiber during the collection process, thus removing the risk of breakage. Easy to operate and low power consumption: the microcontroller, AS7341 spectral sensor, and LED light source have low power consumption, solving the problem of outdoor long-term power supply. This integrated design makes spectrum acquisition more portable and easier to operate and is suitable for spectrum data collection and analysis in outdoor environments, as it is often required for, e.g., agricultural, environmental, and geological purpose. Low cost and maintenance requirements: it has the characteristics of low cost and easy maintenance, which is suitable for some applications with high requirements for cost and maintenance, such as scientific and teaching experiments.

Disadvantages: fewer channels. The AS7341 spectral sensor can collect data from up to 14 channels, while traditional spectrometers can collect data from hundreds of channels. Therefore, the effective resolution of AS7341 data is low, and many effective information may be missed during the collection process, which limits the exploration of spectral data. However, the 14 channels collected are sufficient to support most spectral analysis applications.

In this study, we successfully designed a spectrum data acquisition device and system based on the Internet of Things (IoT) technology. The collection and processing of spectral data were achieved through integrated design and the use of AS7341 spectral sensors and ESP8266 microcontrollers. Our research results show that the device has many advantages, such as portability, ease of operation, and low power consumption, but also some limitations, such as limited channel numbers and low resolution. In future research, we will explore ways to further optimize the performance of the device by using transmission or reflection combined with transmission, in order to meet the demand for higher-precision spectral analysis. At the same time, we will also attempt to improve the light source part to increase the device's collection efficiency and accuracy. In terms of power supply, we will use a battery and device integration design to make data collection more portable. These improvements will help enhance the performance and reliability of the device, thereby providing more accurate and reliable data support for related research.

5. Conclusions

Based on the designed spectral acquisition system and equipment, the spectral data acquisition and SPAD regression prediction analysis of Hami melon leaf samples were completed. The regression analysis results showed that at the wavelength of 515 nm, ETR, RFR, and BAR regression algorithms could all predict SPAD well, among which ETR attained the best prediction effect. On the training set, $RMSE_c$ was 0.3429, and R_c^2 was 0.9905; on the prediction set, $RMSE_p$ was 1.5670, and R_p^2 was 0.8035. After denoising the spectral data, the improvement in prediction accuracy was not significant. Through the use of principal component analysis and Isolation Forest algorithm, abnormal points were successfully detected and removed. After removing the outliers, the prediction accuracy of the dataset, as well as the raw and denoised spectral data, were improved. Among all wavelength combination for spectral data predictions after PBOR denoising, the RFR model performed best. On the training set, $RMSE_c$ was 0.8721 and R_c^2 was 0.9429; on the prediction set, $RMSE_p$ was 1.1810 and R_p^2 was 0.8683. This piece of acquisition

equipment offers several advantages, including small size, convenient portability, cloud access, and real-time visualization of spectral data, providing technical reference value for the development and application of intelligent spectral devices in agriculture.

Author Contributions: L.L. equipment design, construction, and manuscript preparation; J.G. methodology and writing review; Q.W. writing review and editing; J.W. Data curation; Y.L. supervision and writing review; Y.S. investigation and validation. All authors have read and agreed to the published version of the manuscript.

Funding: Project of science and technology innovation team (Tianshan innovation team), Xinjiang smart agricultural information perception technology innovation, 2022TSYCTD0011.

Institutional Review Board Statement: Not applicable.

Informed Consent Statement: Not applicable.

Data Availability Statement: Data available on request from the authors.

Conflicts of Interest: The authors declare no conflict of interest.

Appendix A

Traditional spectrometer section:

(1) Computer: used to read spectral data by the spectral software equipped with the spectrometer, and then save the data in text format such as excel, csv, txt. Its operation interface can only use the spectral software equipped with the spectrometer, and the operating system is restricted, such as only supporting Windows system, etc.
(2) Spectrometer: used to read the spectral data emitted by plant leaves.
(3) Optical fiber: used to transmit spectral data information.
(4) Light source: the lighting device is a halogen lamp, which provides a light source for collecting spectral data.

These four parts are independent parts, and they need to be locally built before they can be used for collection.

Convenient spectrometer section:

(1) Cloud server: receives the spectral data collected by the spectrometer and the data submitted by the user, automatically saves them in the database, and provides remote historical data download and web-based visualization of spectral data functions. Its operation interface provides a web-based visualization interface, making it easy for users to operate across platforms.
(2) Spectrometer: integrated with ESP8266 microcontroller, AS7341 spectral sensor, and LED light source.

These two parts are independent parts, and only a smartphone and a spectrometer are needed to complete the collection work.

Appendix B

The communication test of the spectrum data acquisition device was based on 10 microcontrollers. The test was completed by connecting to a mobile phone's shared network Wi-Fi hotspot. The MQTT topic was "/xjnydx/Spectral", and the JSON format content was transmitted in the manner shown in the key code below. The data was transmitted with a delay of 100 ms for each send and receive cycle. The data was sent from Urumqi, China to a MQTT server in Guiyang, China. This sending method ensured that there was no mutual interference between the data sent and received, and that the microcontroller program would not crash. When the data sent by the microcontroller was not received, the microcontroller would stop the test. Each microcontroller published the data 1010 times, and the data transmission time of the last 1000 pieces of data after collecting 10 pieces of data was taken as the analysis object. The data transmission time was the current data receiving time minus the current data sending time. Through the

completion of 10,100 data transmission tests, there was no data loss. The data communication time test is shown in Figure A1. The maximum data transmission time was found to be 179 ms and the minimum data transmission time was 63 ms through analysis.

```
Key Code:
void publishDate() {
StaticJsonDocument < 128 > doc;
doc["0"] = 1981.09;//415
doc["1"] = 1054.5;//445
doc["2"] = 1098.69;//480
doc["3"] = 703.11;//515
doc["4"] = 607.74;//555
doc["5"] = 1660.49;//590
doc["6"] = 4100.58;//630
doc["7"] = 5216.3;//680
doc["8"] = 5731;//750
doc["9"] = 2511.73;//900
char buffer [128];
serializeJson(doc, buffer);
client.publish("/xjnydx/Spectral", buffer);
}
```

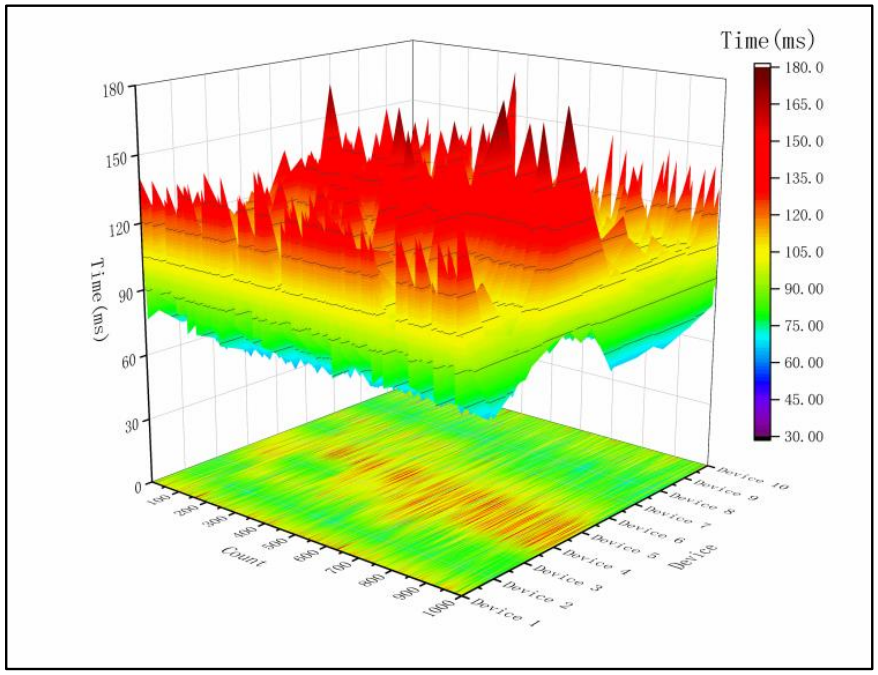

Figure A1. Device data transfer time test.

Appendix C

The time complexity of linear regression (LR) is O(n), and the space complexity is O(n). It is fast when processing large-scale data, but the fitting effect may not be good for data with non-linear relationships. The time complexity of K-nearest neighbor regression (KNN) is O(nm log m), and the space complexity is O(nm). It needs to store all training samples, so it requires a lot of memory when processing large-scale data. In addition, KNN needs to calculate the distance between each test sample and all training samples during prediction, so the prediction speed is slow. The time complexity of support vector regression (SVR) is $O(m^3)$, and the space complexity is $O(m^2)$. It is slow when processing large-scale data, but it has a good fitting effect for data with non-linear relationships. The time complexity of ridge regression (RR) and Lasso regression (Lasso) are both $O(n^3)$, and the space complexity is both $O(n^2)$. It is slow when processing large-scale data, but can handle high-dimensional data and data with multicollinearity. The time complexity of decision tree regression (DTR),

extremely randomized tree regression (ETR), random forest regression (RFR), AdaBoost regression (ABR), gradient boosting regression (GBR), and bagging regression (BAR) are all O(nm log m), and the space complexity is all O(nm). They are fast when processing large-scale data, but may require feature selection or dimensionality reduction when processing high-dimensional data and data with multicollinearity. The time complexity of partial least squares regression (PLSR) is $O(nm^2)$, and the space complexity is O(nm). It is slow when processing large-scale data, but can handle high-dimensional data and data with multicollinearity. Here, n is the number of features, and m is the number of samples.

References

1. Lakshmanna, K.; Kaluri, R.; Gundluru, N.; Alzamil, Z.S.; Rajput, D.S.; Khan, A.A.; Haq, M.A.; Alhussen, A. A Review on Deep Learning Techniques for IoT Data. *Electronics* **2022**, *11*, 1604. [CrossRef]
2. Vincent, B.; Dardenne, P. Application of NIR in Agriculture. In *Near-Infrared Spectroscopy*; Springer Singapore: Singapore, 2021; pp. 331–345.
3. Demattê, J.A.M.; Horák-Terra, I.; Beirigo, R.M.; da Silva Terra, F.; Marques, K.P.P.; Fongaro, C.T.; Silva, A.C.; Vidal-Torrado, P. Genesis and Properties of Wetland Soils by VIS-NIR-SWIR as a Technique for Environmental Monitoring. *J. Environ. Manag.* **2017**, *197*, 50–62. [CrossRef] [PubMed]
4. Amigo, J.M.; Cruz, J.; Bautista, M.; Maspoch, S.; Coello, J.; Blanco, M. Study of Pharmaceutical Samples by NIR Chemical-Image and Multivariate Analysis. *Trends Anal. Chem.* **2008**, *27*, 696–713. [CrossRef]
5. Ma, L.; Peng, Y.; Pei, Y.; Zeng, J.; Shen, H.; Cao, J.; Qiao, Y.; Wu, Z. Systematic Discovery about NIR Spectral Assignment from Chemical Structural Property to Natural Chemical Compounds. *Sci. Rep.* **2019**, *9*, 9503. [CrossRef]
6. Borghi, F.T.; Santos, P.C.; Santos, F.D.; Nascimento, M.H.C.; Corrêa, T.; Cesconetto, M.; Pires, A.A.; Ribeiro, A.V.F.N.; Lacerda, V.; Romão, W.; et al. Quantification and Classification of Vegetable Oils in Extra Virgin Olive Oil Samples Using a Portable Near-Infrared Spectrometer Associated with Chemometrics. *Microchem. J.* **2020**, *159*, 105544. [CrossRef]
7. Liu, J.; Han, J.; Chen, X.; Shi, L.; Zhang, L. Nondestructive Detection of Rape Leaf Chlorophyll Level Based on Vis-NIR Spectroscopy. *Spectrochim. Acta A Mol. Biomol. Spectrosc.* **2019**, *222*, 117202. [CrossRef]
8. Wang, B.; He, X.; Bi, Y.; Jiang, H.; Wang, Y.; Zheng, X.; Prusky, D. Preharvest Sprays with Sodium Nitroprusside Induce Resistance in Harvested Muskmelon against the Pink Rot Disease. *J. Food Process Preserv.* **2021**, *45*, e15339. [CrossRef]
9. Takai, T.; Adachi, S.; Taguchi-Shiobara, F.; Sanoh-Arai, Y.; Iwasawa, N.; Yoshinaga, S.; Hirose, S.; Taniguchi, Y.; Yamanouchi, U.; Wu, J.; et al. A Natural Variant of NAL1, Selected in High-Yield Rice Breeding Programs, Pleiotropically Increases Photosynthesis Rate. *Sci. Rep.* **2013**, *3*, 2149. [CrossRef]
10. Peng, J.; Feng, Y.; Wang, X.; Li, J.; Xu, G.; Phonenasay, S.; Luo, Q.; Han, Z.; Lu, W. Effects of Nitrogen Application Rate on the Photosynthetic Pigment, Leaf Fluorescence Characteristics, and Yield of Indica Hybrid Rice and Their Interrelations. *Sci. Rep.* **2021**, *11*, 7485. [CrossRef]
11. Xu, Q.; Ma, X.; Lv, T.; Bai, M.; Wang, Z.; Niu, J. Effects of Water Stress on Fluorescence Parameters and Photosynthetic Characteristics of Drip Irrigation in Rice. *Water* **2020**, *12*, 289. [CrossRef]
12. Zheng, J.; Song, X.; Yang, G.; Du, X.; Mei, X.; Yang, X. Remote Sensing Monitoring of Rice and Wheat Canopy Nitrogen: A Review. *Remote Sens.* **2022**, *14*, 5712. [CrossRef]
13. Mistele, B.; Schmidhalter, U. Estimating the Nitrogen Nutrition Index Using Spectral Canopy Reflectance Measurements. *Eur. J. Agron.* **2008**, *29*, 184–190. [CrossRef]
14. Prananto, J.A.; Minasny, B.; Weaver, T. Rapid and Cost-Effective Nutrient Content Analysis of Cotton Leaves Using Near-Infrared Spectroscopy (NIRS). *PeerJ* **2021**, *9*, e11042. [CrossRef] [PubMed]
15. Liu, L.; Zareef, M.; Wang, Z.; Li, H.; Chen, Q.; Ouyang, Q. Monitoring Chlorophyll Changes during Tencha Processing Using Portable Near-Infrared Spectroscopy. *Food Chem.* **2023**, *412*, 135505. [CrossRef] [PubMed]
16. Zhang, J.; Han, W.; Huang, L.; Zhang, Z.; Ma, Y.; Hu, Y. Leaf Chlorophyll Content Estimation of Winter Wheat Based on Visible and Near-Infrared Sensors. *Sensors* **2016**, *16*, 437. [CrossRef]
17. Wang, Y.-J.; Jin, S.-S.; Li, M.-H.; Liu, Y.; Li, L.-Q.; Ning, J.-M.; Zhang, Z.-Z. Onsite Nutritional Diagnosis of Tea Plants Using Micro Near-Infrared Spectrometer Coupled with Chemometrics. *Comput. Electron. Agric.* **2020**, *175*, 105538. [CrossRef]
18. Jin, X.; Wang, L.; Zheng, W.; Zhang, X.; Liu, L.; Li, S.; Rao, Y.; Xuan, J. Predicting the Nutrition Deficiency of Fresh Pear Leaves with a Miniature Near-Infrared Spectrometer in the Laboratory. *Measurement* **2022**, *188*, 110553. [CrossRef]
19. Lee, Y.-H.; Sang, W.-G.; Baek, J.-K.; Kim, J.-H.; Shin, P.; Seo, M.-C.; Cho, J.-I. The Effect of Concurrent Elevation in CO_2 and Temperature on the Growth, Photosynthesis, and Yield of Potato Crops. *PLoS ONE* **2020**, *15*, e0241081. [CrossRef]
20. Song, D.; Gao, D.; Sun, H.; Qiao, L.; Zhao, R.; Tang, W.; Li, M. Chlorophyll Content Estimation Based on Cascade Spectral Optimizations of Interval and Wavelength Characteristics. *Comput. Electron. Agric.* **2021**, *189*, 106413. [CrossRef]
21. Pampolino, M.F.; Witt, C.; Pasuquin, J.M.; Johnston, A.; Fisher, M.J. Development Approach and Evaluation of the Nutrient Expert Software for Nutrient Management in Cereal Crops. *Comput. Electron. Agric.* **2012**, *88*, 103–110. [CrossRef]
22. Elavarasan, D.; Vincent, P.M.D.R.; Srinivasan, K.; Chang, C.-Y. A Hybrid CFS Filter and RF-RFE Wrapper-Based Feature Extraction for Enhanced Agricultural Crop Yield Prediction Modeling. *Agriculture* **2020**, *10*, 400. [CrossRef]

23. Dong, T.; Shang, J.; Chen, J.M.; Liu, J.; Qian, B.; Ma, B.; Morrison, M.J.; Zhang, C.; Liu, Y.; Shi, Y.; et al. Assessment of Portable Chlorophyll Meters for Measuring Crop Leaf Chlorophyll Concentration. *Remote Sens.* **2019**, *11*, 2706. [CrossRef]
24. Gutiérrez, S.; Tardaguila, J.; Fernández-Novales, J.; Diago, M.P. Support Vector Machine and Artificial Neural Network Models for the Classification of Grapevine Varieties Using a Portable NIR Spectrophotometer. *PLoS ONE* **2015**, *10*, e0143197. [CrossRef]
25. Barbon Junior, S.; Mastelini, S.M.; Barbon, A.P.A.C.; Barbin, D.F.; Calvini, R.; Lopes, J.F.; Ulrici, A. Multi-Target Prediction of Wheat Flour Quality Parameters with Near Infrared Spectroscopy. *Inf. Process. Agric.* **2020**, *7*, 342–354. [CrossRef]
26. Hou, B.; Hu, Y.; Zhang, P.; Hou, L. Potato Late Blight Severity and Epidemic Period Prediction Based on Vis/NIR Spectroscopy. *Agriculture* **2022**, *12*, 897. [CrossRef]
27. Wang, J.; Zhou, Q.; Shang, J.; Liu, C.; Zhuang, T.; Ding, J.; Xian, Y.; Zhao, L.; Wang, W.; Zhou, G.; et al. UAV- and Machine Learning-Based Retrieval of Wheat SPAD Values at the Overwintering Stage for Variety Screening. *Remote Sens.* **2021**, *13*, 5166. [CrossRef]
28. Li, Y.; Xia, H.; Liu, Y.; Huo, L.; Ni, C.; Gou, B. Detection of Moisture Content of *Pinus massoniana* Lamb. Seedling Leaf Based on NIR Spectroscopy with a Multi-Learner Model. *Forests* **2023**, *14*, 883. [CrossRef]
29. Yang, Y.; Nan, R.; Mi, T.; Song, Y.; Shi, F.; Liu, X.; Wang, Y.; Sun, F.; Xi, Y.; Zhang, C. Rapid and Nondestructive Evaluation of Wheat Chlorophyll under Drought Stress Using Hyperspectral Imaging. *Int. J. Mol. Sci.* **2023**, *24*, 5825. [CrossRef]
30. Zhang, M.; Chen, T.; Gu, X.; Kuai, Y.; Wang, C.; Chen, D.; Zhao, C. UAV-Borne Hyperspectral Estimation of Nitrogen Content in Tobacco Leaves Based on Ensemble Learning Methods. *Comput. Electron. Agric.* **2023**, *211*, 108008. [CrossRef]
31. Zhang, J.; Zhang, W.; Xiong, S.; Song, Z.; Tian, W.; Shi, L.; Ma, X. Comparison of New Hyperspectral Index and Machine Learning Models for Prediction of Winter Wheat Leaf Water Content. *Plant Methods* **2021**, *17*, 34. [CrossRef]
32. Yuan, Z.; Ye, Y.; Wei, L.; Yang, X.; Huang, C. Study on the Optimization of Hyperspectral Characteristic Bands Combined with Monitoring and Visualization of Pepper Leaf SPAD Value. *Sensors* **2021**, *22*, 183. [CrossRef] [PubMed]
33. Wang, J.; Xue, W.; Shi, X.; Xu, Y.; Dong, C. Adaboost-Based Machine Learning Improved the Modeling Robust and Estimation Accuracy of Pear Leaf Nitrogen Concentration by In-Field VIS-NIR Spectroscopy. *Sensors* **2021**, *21*, 6260. [CrossRef]
34. Wu, Q.; Zhang, Y.; Xie, M.; Zhao, Z.; Yang, L.; Liu, J.; Hou, D. Estimation of Fv/Fm in Spring Wheat Using UAV-Based Multispectral and RGB Imagery with Multiple Machine Learning Methods. *Agronomy* **2023**, *13*, 1003. [CrossRef]
35. Qu, F.; Ren, D.; Wang, J.; Zhang, Z.; Lu, N.; Meng, L. An Ensemble Successive Project Algorithm for Liquor Detection Using Near Infrared Sensor. *Sensors* **2016**, *16*, 89. [CrossRef] [PubMed]
36. Zhang, J.; Liu, Z.; Pu, Y.; Wang, J.; Tang, B.; Dai, L.; Yu, S.; Chen, R. Identification of Transgenic Agricultural Products and Foods Using NIR Spectroscopy and Hyperspectral Imaging: A Review. *Processes* **2023**, *11*, 651. [CrossRef]
37. Shen, S.; Hua, J.; Zhu, H.; Yang, Y.; Deng, Y.; Li, J.; Yuan, H.; Wang, J.; Zhu, J.; Jiang, Y. Rapid and Real-Time Detection of Moisture in Black Tea during Withering Using Micro-Near-Infrared Spectroscopy. *LWT* **2022**, *155*, 112970. [CrossRef]
38. Golhani, K.; Balasundram, S.K.; Vadamalai, G.; Pradhan, B. Estimating Chlorophyll Content at Leaf Scale in Viroid-Inoculated Oil Palm Seedlings (*Elaeis guineensis* Jacq.) Using Reflectance Spectra (400 Nm–1050 Nm). *Int. J. Remote Sens.* **2019**, *40*, 7647–7662. [CrossRef]
39. Bao, Y.; Kong, W.; He, Y.; Liu, F.; Tian, T.; Zhou, W. Quantitative Analysis of Total Amino Acid in Barley Leaves under Herbicide Stress Using Spectroscopic Technology and Chemometrics. *Sensors* **2012**, *12*, 13393–13401. [CrossRef]
40. Li, F.; Wang, L.; Liu, J.; Wang, Y.; Chang, Q. Evaluation of Leaf N Concentration in Winter Wheat Based on Discrete Wavelet Transform Analysis. *Remote Sens.* **2019**, *11*, 1331. [CrossRef]
41. Jahani, S.; Setarehdan, S.K.; Boas, D.A.; Yücel, M.A. Motion Artifact Detection and Correction in Functional Near-Infrared Spectroscopy: A New Hybrid Method Based on Spline Interpolation Method and Savitzky–Golay Filtering. *Neurophotonics* **2018**, *5*, 1. [CrossRef]
42. Amariei, G.; Henriksen, M.L.; Friis, J.B.; Pedersen, P.K.; Hinge, M. In-Line Identification of Pb-Based Pigments in Fishing Nets and Ropes Based on Hyperspectral Imaging and Machine Learning. *Mar. Pollut. Bull.* **2023**, *191*, 114910. [CrossRef]
43. Carlomagno, G.; Capozzo, L.; Attolico, G.; Distante, A. Non-Destructive Grading of Peaches by Near-Infrared Spectrometry. *Infrared Phys. Technol.* **2004**, *46*, 23–29. [CrossRef]
44. Li, J.S.; Hamann, A.; Beaubien, E. Outlier Detection Methods to Improve the Quality of Citizen Science Data. *Int. J. Biometeorol.* **2020**, *64*, 1825–1833. [CrossRef] [PubMed]
45. Viscarra Rossel, R.A.; Cattle, S.R.; Ortega, A.; Fouad, Y. In Situ Measurements of Soil Colour, Mineral Composition and Clay Content by Vis–NIR Spectroscopy. *Geoderma* **2009**, *150*, 253–266. [CrossRef]
46. Kamruzzaman, M.; ElMasry, G.; Sun, D.-W.; Allen, P. Application of NIR Hyperspectral Imaging for Discrimination of Lamb Muscles. *J. Food Eng.* **2011**, *104*, 332–340. [CrossRef]
47. Huang, H.; Hu, X.; Tian, J.; Peng, X.; Luo, H.; Huang, D.; Zheng, J.; Wang, H. Rapid and Nondestructive Determination of Sorghum Purity Combined with Deep Forest and Near-Infrared Hyperspectral Imaging. *Food Chem.* **2022**, *377*, 131981. [CrossRef]